Relative Effects of Velocity- and Mixture-Coupling in a Thermoacoustically Unstable, Partially-Premixed Flame

Ashwini Karmarkar,
Department of Mechanical Engineering
Pennsylvania State University
University Park, PA, USA
auk1002@psu.edu

Isaac Boxx
DLR - German Aerospace Center
Stuttgart, Germany
isaac.boxx@dlr.de

Jacqueline O'Connor*
Department of Mechanical Engineering
Pennsylvania State University
University Park, PA, USA
jxo22@psu.edu

ABSTRACT

Combustion instability, which is the result of a coupling between combustor acoustic modes and unsteady flame heat release rate, is a severely limiting factor in the operability and performance of modern gas turbine engines. This coupling can occur through different coupling pathways, such as flow field fluctuations or equivalence ratio fluctuations. In realistic combustor systems, there are complex hydrodynamic and thermo-chemical processes involved, which can lead to multiple coupling pathways. In order to understand and predict the mechanisms that govern the onset of combustion instability in real gas turbine engines, we consider the influences that each of these coupling pathways can have on the stability and dynamics of a partially-premixed, swirl-stabilized flame. In this study, we use a model gas turbine combustor with two concentric swirling nozzles of air, separated

*Address all correspondence to this author.

by a ring of fuel injectors, operating at an elevated pressure of 5 bar. The flow split between the two streams is systematically varied to observe the impact on the flow and flame dynamics. High-speed stereoscopic particle image velocimetry, OH planar laser-induced fluorescence, and acetone planar laser-induced fluorescence are used to obtain information about the velocity field, flame, and fuel-flow behavior, respectively. Depending on the flow conditions, a thermoacoustic oscillation mode or a hydrodynamic mode, identified as the precessing vortex core, is present. The focus of this study is to characterize the mixture coupling processes in this partially-premixed flame as well as the impact that the velocity oscillations have on mixture coupling. Our results show that, for this combustor system, changing the flow split between the two concentric nozzles can alter the dominant harmonic oscillation modes in the system, which can significantly impact the dispersion of fuel into air, thereby modulating the local equivalence ratio of the flame. This insight can be used to design instability control mechanisms in real gas turbine engines.

NOMENCLATURE

C Open contour tracing the flame edge

$G_{\psi_R \psi_L}$ Cross-spectral density

L_f Total flame length

PLIF Planar laser-induced fluorescence

PMT Photomultiplier tube

PSD Power spectral density

PVC Precessing vortex core

Re Reynolds number

T Temperature

$\vec{V}$ Instantaneous velocity field

dl_f Elemental flame edge length

$\hat{n}$ Unit vector normal to the flame edge

u Velocity

r Cross-stream coordinate

z Streamwise coordinate

Φ Fuel flux calculated along the flame edge

ϕ Global equivalence ratio

ψ Signal intensity of acetone LIF signal

INTRODUCTION

Restrictions on NO_x emissions have driven a technology shift towards lean premixed combustion in power generation gas turbine engines. While lean premixed systems have been successful at reducing emissions, lean flames are generally less stable and hence susceptible to external perturbations, which can restrict combustor operability. In particular, the onset of combustion instability has been shown to be a severely limiting factor to the operability of gas turbine engines [1].

Combustion instability is a thermoacoustic instability arising from the coupling between resonant acoustic modes of the combustor and the unsteady rate of heat release from the flame, which can lead to large scale oscillations in the flow field of the combustor [2]. These oscillations can cause increased emissions, structural damage, and, in extreme cases, engine failure. Figure 1 schematically shows the feedback loop driving thermoacoustic instability. The coupling between acoustic modes and flame heat release rate can occur through fluctuations in pressure, velocity, or fuel flow rate. In partially-premixed combustors, such as the configuration studied in this work, multiple coupling mechanisms may be active, which can lead to potential interaction between the coupling mechanisms. As such, it is important to understand the influence of these mechanisms on each other and on the structure and stability of the flame.

Equivalence ratio fluctuations have been shown to drive combustion instabilities in partially-premixed or non-premixed combustors [3–7]. Pressure oscillations in the combustor interact with the fuel supply and cause coherent oscillations in the equivalence ratio of the reactant mixture, which when convected to the flame, can cause pulsations in the heat release rate. Lee et al. [8] have shown, using an infrared absorption technique for measuring equivalence ratio fluctuations, that the equivalence ratio fluctuations are strongly linked to the heat release fluctuations in an un-

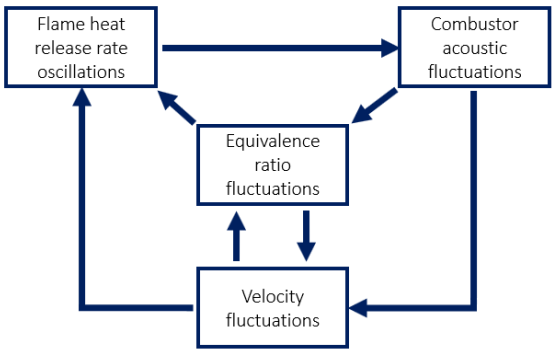

Fig. 1. Combustion instability feedback loop

stable combustor and can thereby play a significant role in driving the instability. In an experimental study conducted in a realistic, swirl-stabilized combustor configuration, Stöhr et al. [9] analyzed the fluctuations in fuel-air ratio by using acetone as a tracer in the fuel, similar to the technique used in this study.

Velocity coupling mechanisms of combustion instability are often driven by large-scale coherent structures distorting the flame and altering the heat release rate [10–14]. It has been shown, in several configurations, that large-scale vortices entrain fresh reactants and can cause the flame to roll-up, thereby sharply increasing its surface area and creating heat release pulses [15–17]. This coherent pulsation of heat release rate feeds back into the acoustic pressure oscillation, thereby completing the feedback loop and causing a sustained instability. Poinsot et al. [12] proposed a detailed mechanism for flame-vortex interaction and showed how the generation of vortices can be the the driving mechanism behind combustion instability.

While in many thermoacoustic instabilities vortex shedding is driven by the acoustic oscillations, inherent hydrodynamic instabilities can also be the source of large-scale vortical motion in combustor flows. Modern combustors often use swirling flows to stabilize lean flames because of a phenomenon known as vortex breakdown [18, 19], which is characterized by the formation of a central recirculation zone or vortex breakdown bubble. Vortex breakdown occurs in highly swirling flows as a result of a collapse in the flow driven by the large radial pressure gradient that arises from swirl [20]. In combustors, the occurrence of this breakdown bubble depends largely on the swirl number and the combustor configuration, particularly the dump ratio (ratio of the combustor

area to the nozzle area) and the combustor exit boundary condition [21]. The recirculation zone constantly supplies hot gases and active radicals to the base of the flame, enhancing its static stability [22]. In some cases, the swirling flow can be globally unstable and drive the vortex breakdown bubble to precess about the central axis, forming what is known as a precessing vortex core (PVC). The PVC is a self-excited global instability that leads to large-scale helical disturbances in the flow field [23, 24]; recent work by Manoharan et al. [25] used weakly nonlinear hydrodynamic stability analysis to show that the precessing vortex core arises from a center mode in the flow that becomes globally unstable with the onset of recirculation from vortex breakdown. In combustor systems, the amplitude of a PVC is a function of swirl number, flame shape, fuel/air mixing, combustor configuration, and equivalence ratio [21].

Stöhr et al. [26] have shown how the shear-layer vortices generated by a precessing vortex core can cause large-scale flame roll-up and couple with the unsteady heat release. Their analysis shows that the PVC drives precession of the upstream stagnation point about the central axis. This stagnation point is the location where burned gases come into contact with the reactant mixture, thereby creating a precessing 'ignition source,' which enhances flame stability. Frederick et al. [27] showed, using experiments and linear stability analysis, that the PVC can suppress shear layer receptivity to longitudinal acoustic modes in a non-reacting swirling flow at a range of swirl numbers. This result is significant because the suppression of coherent velocity fluctuations that modulate the flame at the acoustic frequency can be a direct method of suppressing combustion instability.

In swirl-stabilized combustors, both thermoacoustic oscillations and hydrodynamic instability in the form of PVC can be present and their interaction with each other and their impact on the flame is strongly influenced by the combustor configuration and the nature of the base flow. The PVC has been shown to undergo axial extension and contraction at the thermoacoustic frequency [28]. Furthermore, experimental studies have also reported the presence of a spectral peak at an interaction frequency that corresponds to the difference between the PVC and thermoacoustic frequencies, which is likely a consequence of nonlinear phenomena [28, 29].

In another study, performed on the same data set as the current study [30], we showed that in

cases where the frequency of the PVC overlaps with the frequency of the thermoacoustic mode, the thermoacoustic oscillation is suppressed and the PVC is the dominant coherent motion in the flow. Weakly nonlinear asymptotic analysis of the system identified the mechanism by which this nonlinear suppression of the thermoacoustic mode by the PVC is possible. In this study, the data show that while the flame motion is synchronized with the PVC oscillation when the PVC is present, the fuel flow fluctuation does not synchronize to the PVC oscillation. We show that when the thermoacoustic mode is active, both velocity- and mixture-coupling pathways are present in the flow through spectral analysis of the velocity field and the fuel flow rate; in this case, the flame motion is symmetric in response to the longitudinal oscillations of the thermoacoustic mode. Furthermore, using fuel flux computed along the instantaneous flame edge as a quantitative metric, we look at the coupling between the velocity and equivalence ratio coupling mechanisms at different levels of thermoacoustic instability. When the thermoacoustic instability is suppressed by the PVC, the flame behavior tracks that of the PVC, displaying anti-symmetric motion. However, the fuel flow rate does not fluctuate at the PVC frequency, cutting off any mixture-coupling processes at the new dominant mode.

EXPERIMENTAL METHODS

Experiment

Experiments were conducted in a $68 \times 68 \times 120$ mm^2 combustion chamber with optical access on four sides, as shown in Fig. 2. A dual-annular swirler is fed with room-temperature air, where the outer swirler has a 14.4 mm inner diameter and a 19.8 mm outer diameter, and the inner swirler has a 12.3 mm diameter. Gaseous ethylene is injected into fuel-injection slots between these two swirler passages. The exhaust consists of a cylindrical cross-section with a 40 mm diameter and a 24 mm length. The combustion chamber is located in a high-pressure vessel at an operating pressure of 5 bar. A dynamic pressure transducer is located at the downstream end of the combustor to monitor thermoacoustic instability in the system. A more detailed discussion of the experimental facility, including more images of the experiment, exhaust, and injector, is found in Geigle et al. [31].

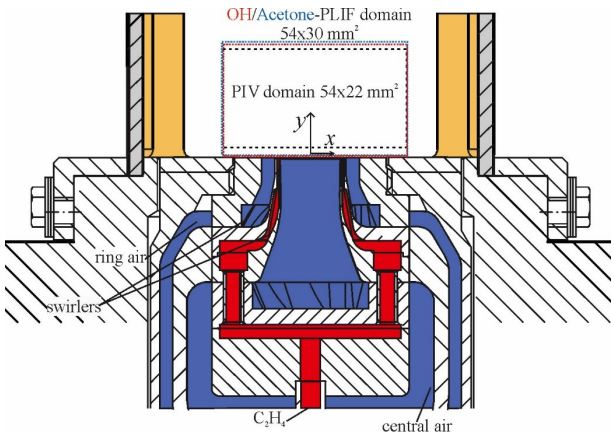

Fig. 2. Experimental setup with fields of view for three diagnostics.

The total air flow rate in each of the cases is 841.7 SLM, resulting in a Reynolds number of $Re = 25,903$ based on inner-swirler diameter. The fuel flow rate is 37.9 SLM, with a global equivalence ratio of $\phi = 0.67$ and a thermal load of 38.4 kW. The flows of air and fuel were supplied by separate mass flow controllers (Bronkhorst). The flow controllers were calibrated in-house, resulting in an accuracy of better than 1.0% of the controllers' maximum flow. The total air flow is divided between the two swirler passages, where the *air split* is defined as the ratio of the mass flow rate of air through the central nozzle to the total mass flow rate of air; it is varied between 0.2 to 0.5 in increments of 0.05. The inner swirler has a geometric swirl number of 0.82 and the outer swirler has a geometric swirl number of 0.79. Given the similarity between the swirl numbers of both swirlers, variations in air split do not significantly change the swirl number of the flow.

Diagnostics

Velocity fields were measured using a two-camera, stereoscopic particle image velocimetry (sPIV) system. The sPIV system used a dual-cavity, diode-pumped, solid state laser (Edgewave, IS200-2-LD, up to 9 mJ/pulse at 532 nm) and a pair of highspeed CMOS cameras (Phantom V1212). PIV image pairs were acquired at 10 kHz and 640$\times$ 800 pixel resolution. The PIV measurement domain spans across most of the width of the combustion chamber (-27 mm $< r <$27 mm). In the axial direction, the domain spans 5 mm$< z <$ 27 mm, as shown in Fig. 2. Time

separation of the laser pulses was $\delta t = 10\mu s$. The beam was formed into a sheet using a pair of cylindrical lenses ($f = -38$ mm and 250 mm) and thinned to a waist using a third cylindrical lens ($f = 700$ mm). Both combustion air flows were seeded with titanium dioxide (TiO_2) particles of nominal diameter 0.5 μm. Image mapping, calibration, and particle cross-correlations were completed using a commercial, multi-pass adaptive window offset cross-correlation algorithm (LaVision DaVis 8.4). Final interrogation window size and overlap were 24$\times$24 pixels and 50%, respectively, for a spatial resolution of 1.9 mm and vector spacing of 0.95 mm. The absolute values of uncertainty of instantaneous velocities based on the correlation statistics in DaVis were estimated to be 0.1 m/s–1.1 m/s for the in-plane components (r-z plane) and 0.3 m/s–2.3 m/s for the out-of-plane component. On average, uncertainty values for the in-plane components are in the range of 0.04 m/s–0.45 m/s and the uncertainty values for the out-of-plane component are in the range of 0.10 m/s–0.9 m/s.

The flame is tracked using planar laser-induced fluorescence of OH (OH-PLIF) and the fuel injection is tracked using planar laser-induced fluorescence of acetone. The majority of the ethylene flow was bubbled through a temperature-controlled reservoir (T=25°C, 298 K) filled with acetone, which provided an acetone-saturated ethylene flow of the desired composition. The OH-/acetone-PLIF imaging system consists of a frequency-doubled dye laser, pumped by a high-speed, pulsed Nd:YAG laser (Edgewave IS400-2-L, 135 W at 532 nm and 10 kHz), and a pair of intensified high-speed CMOS camera systems. The dye laser system (Sirah Credo) produced 5.3—5.5 W at 283 nm and a 10 kHz repetition rate (i.e. 0.53–0.55 mJ/pulse). The dye laser was tuned to excite the Q1(9) and Q2(8) lines of the $A^2\Sigma^+ - X^2\Pi(v' = 1, v'' = 0)$ band. These transitions merge at high pressure due to increased collisional line broadening, which mitigates to some degree fluorescence signal loss due to collisional line broadening. The laser wavelength was monitored continuously throughout the experiments using a photomultiplier tube (PMT) mounted to a 10 cm monochrometer and a premixed, laminar reference flame. The 283 nm PLIF excitation beam is formed into a sheet approximately 40 mm (high) x 0.2 mm (thick) using three fused-silica, cylindrical lenses (all anti-reflective coated to maximize transmission). The laser sheets of the OH-/acetone-PLIF and PIV systems were overlapped by passing the (green, 532 nm) PIV sheet

through the final OH-PLIF turning mirror.

The same laser was used to excite fluorescence signal in both the OH- and the acetone-PLIF imaging systems. For acetone-PLIF, fluorescence signal was imaged with a CMOS camera (LaVision HSS8), an external two-stage intensifier (LaVision HS-IRO), equipped with 85 mm focal length, $f/1.2$ (Canon) objective and a band pass interference filter. The filter (LOT, 450FS40-50) was centered at 450 nm for detection of the acetone fluorescence and had a bandpass of ± 20 nm. OH-PLIF fluorescence signal was imaged using a similar highspeed CMOS camera (LaVision HSS8) and external two-stage intensifier (LaVision HS-IRO) from the opposite side of the combustor. The OH-PLIF camera was equipped with 64 mm focal length, $f/2$ (Halle) UV-objective and a high transmission bandpass interference filter. The OH/acetone-PLIF measurement domain was slightly larger than that of the PIV system, spanning (-27 mm$< r <$27 mm, 0 mm$< z <$ 30 mm), as shown in Fig. 2. Both the PIV and PLIF sampling rates were 10 kHz and 10,000 images were taken at each condition, resulting in a spectral resolution of 1 Hz and a maximum resolved frequency of 5000 Hz for these data.

Previous studies have demonstrated the feasibility of using acetone as fuel tracer in a dual-swirl gas turbine model combustor similar to that used in the present study [9, 32]. These studies indicated that replacement of 10% vol of the original (methane) fuel by acetone vapor did not significantly change the flame shape or dynamics. Although the present study uses ethylene rather than methane, it is expected to have a similarly negligible effect on the flame shape and dynamics.

The intensity of signal from the fluorescence of acetone was calibrated over a range of equivalence ratios, from 0.2 to 3. The signal intensity seen at an equivalence ratio of 0.2 is comparable to the intensity of signal noise and, as such, fuel concentrations below an equivalence ratio 0.2 cannot be reliably measured. The signal intensity of the acetone in the regions analyzed in this work – on the reactant side of the flame and at the fuel injection location – is well within the range of detection and is therefore usable for analysis. Despite the calibration, this work does not attempt to quantify the instantaneous equivalence ratio of the fuel/air mixture at any point in time; all the analysis considers the fluctuation level of the acetone signal in different regions of the field of view.

DATA ANALYSIS

Spectral analysis

Combustor dynamic pressure was measured at a sampling rate of 1 MHz over a period of 2 seconds. The pressure spectra are ensemble-averaged over ten ensembles, leading to a spectral resolution of 5 Hz on the power spectral densities of the pressure fluctuation.

In a realistic combustor, such as the one studied in this work, multiple harmonic oscillations can be simultaneously present, resulting in multiple peaks in frequency-domain analysis of signals from the combustor. In particular, the flow field can display multiple modes of oscillation, including those that are acoustically excited as well as those that are self-excited due to hydrodynamic instability [28]. To understand the spatio-temporal nature of each oscillation, we perform a Fourier reconstruction of the velocity fields around each of the peak frequencies in a velocity field spectrum. This is done by calculating the linear spectrum using the Fourier transform of the fluctuation in the velocity signal at each vector in space, isolating the value of the linear spectrum at individual peak frequencies, and then calculating the inverse transform of the signal at this peak frequency to yield a time-domain signal at each point in space. Essentially, the process is equivalent to frequency-domain filtering the signal using a narrow bandpass filter centered around a given frequency of interest. The result of this analysis provides time-domain oscillations at just one frequency where the phase information for each velocity vector is retained, allowing for analysis of the spatial structure of an oscillation at a given frequency. This method is more precise than a time-domain filter, which can have adverse effects on phase, or a method like proper orthogonal decomposition (POD), which is energy-ordered rather than dependent on frequency. For more detailed analysis of this flow field using spectral proper orthogonal decomposition (SPOD) to understand hydrodynamic instabilities, see our companion work in Ref. [30].

To understand the dynamics of the fuel flow at the point of injection, we perform a cross spectral density calculation on the acetone-PLIF signal between the left and the right branches. The magnitude of the cross-spectrum is equal to the product of the magnitudes of the linear spectra of each of the two time series and the phase of the cross-spectrum is equal to the phase difference between the two signals. This information is useful for quantifying the amplitude and symmetry of

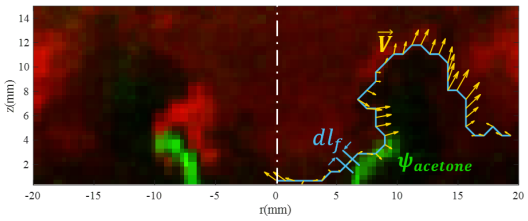

Fig. 3. Instantaneous snapshot of superimposed flame from OH-PLIF (red) and fuel flow from acetone-PLIF (green).The blue line contour indicates the instantaneous flame edge and the velocity vectors along the edge are depicted by yellow arrows.

the oscillations in the fuel flow. The fuel flow signal is calculated by extracting the time series of the peak acetone signal at the dump plane, where the fuel is injected, in each branch. The signal is averaged over a 3 pixel $\times$ 3 pixel interrogation window to avoid spurious results that can appear while conducting point-wise measurements. The two time series are then used to compute the cross spectral density as a function of frequency.

Flame edge analysis

The OH-PLIF signal is used to characterize the flame behavior. To study the oscillation of the flame and its interaction with the fuel and velocity fields, the flame edge must be identified. Here, we assume that the flame edge can be defined at the edge of the OH-PLIF signal. In a fully-premixed flame, the flame edge could be identified using a maximum gradient definition from an OH-PLIF image [33]. In a non-premixed flame, the flame is typically identified using maximum OH-PLIF signals [34]. As this is a partially-premixed flame and the acetone-PLIF images show that there is good mixing of fuel and air ahead of the OH-PLIF signal (based on the acetone-PLIF calibration discussed previously), we use a fully-premixed flame edge definition in analyzing the OH-PLIF.

The raw OH-PLIF images are first filtered using a bilateral filter to remove noise and smooth sharp gradients. The images are then binarized using a multi-level thresholding function, `multithresh` in MATLAB, where the reactant regions are assigned a value of zero and the products are assigned a value of 1. The thresholds are calculated using Otsu's method and a maximum of four levels are used for the binarization. The flame edge is then calculated by tracing the edges of the binary image using the `bwboundaries` function in MATLAB. Figure 3 shows an instantaneous snapshot

image of the superimposed OH-PLIF image (red contour) with the acetone-PLIF image (green contour). The original image is shown on the left, and the instantaneous flame edge is depicted using the blue line contour on the right.

To characterize the oscillation of the flame edge and fluctuations in the flame surface area, the total flame edge length, L_f, is used as a quantitative metric. Flame length is defined in equation 1, where C is a contour tracing the flame edge and dl_f is the elemental flame edge length, as shown in Fig.3.

$$L_f = \int_C dl_f \tag{1}$$

The analysis was conducted on both the left and right sides of the frame and the results were found to be largely identical. However, the image quality is better on the right side of the images, as the laser propagated from right-to-left for the LIF imaging, and so flame edge identification is more robust. For these reasons, the flame edge results presented in this study will pertain to the right branch of the flame.

Fuel flux analysis

In order to quantitatively understand the influence of the equivalence ratio coupling mechanism on the flame and its interaction with the velocity coupling mechanism, we compute the flux of the fuel into the flame at every instant using the acetone-PLIF signal intensity, $\psi_{acetone}$, the flame edge obtained from the binary OH-PLIF images, and the velocity vectors obtained from the PIV data. The signal is not always defined along the entire flame edge contour given the partially-premixed nature of the system, which can introduce noise into the flux calculation. However, since the focus of this analysis is to study the frequency domain behavior of the signal and not the absolute flux magnitude, the additional noise will not significantly impact detection of the dominant oscillation mode. The total fuel flux, Φ, is defined as the integral of the acetone signal multiplied by the velocity normal to the flame, integrated over the flame length, a shown by equation 2, where C

denotes the open contour tracing the flame edge, $\vec{V}$ is the velocity vector, depicted by the yellow arrows in Fig. 3, $\hat{n}$ is the unit vector normal to the flame edge (not shown), and dl_f is the elemental flame length.

$$\Phi = \int_C \psi_{acetone}(\vec{V}.\hat{n})dl_f \tag{2}$$

To be more precise, the velocity used for the flux calculation should be the relative velocity between the flame and the flow, as this flame is likely premixed enough to propagate. This calculation would require quantification of the flame displacement in time in addition to the flow velocity normal to the flame, as done by Trunk et al. [35] using dual-plane PLIF. Since this a two-dimensional data set, however, the uncertainties incurred in attempting these calculations would be significant. Additionally, we believe that the *fluctuating* behaviors, which are reported here and critical to our understanding of the velocity- and mixture-coupling mechanisms, will not be significantly impacted by considering this calculation in two dimensions and ignoring the flame propagation component. As such, using the acetone signal intensity and the velocity data to compute influx of fuel to the flame can provide valuable insight.

RESULTS

Time-averaged profiles

The time-averaged streamwise velocity profiles for several air split conditions are shown in the right column of Fig.4, with the white lines indicating the streamlines calculated from time-averaged velocity vectors. We show a subset of the data here for brevity, but the trends in the structure of the flow with air split are monotonic. In all cases, a region of reverse flow can be seen near the center of the flow, which is indicative of vortex breakdown [19]. In this flow, the recirculation zone grows in size and strength as the air split increases. Recirculation strength, indicated by the maximum reverse velocity along the centerline of the recirculation zone, is significantly higher for the air split of 0.5 relative to the air split of 0.2. Details of the theoretical basis for this change in flow structure

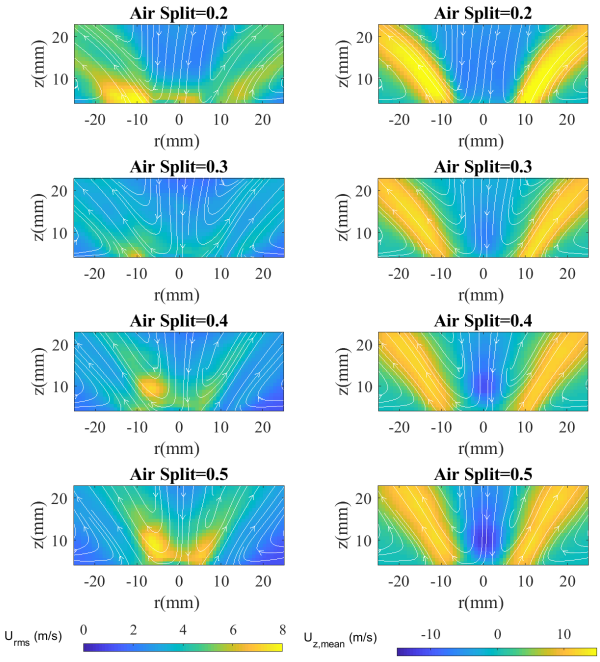

Fig. 4. RMS of the velocity field fluctuation (left) and time-averaged streamwise velocity (right) for varying air split conditions.

are discussed in Karmarkar et al. [30].

The RMS profiles of the velocity fluctuation at varying air split conditions are shown in the left column Fig. 4 as an illustration of turbulence intensity of the flow. While the location of the maximum RMS region shifts from the outer shear layer to the inner shear layer as the air split increases, the mean value of the RMS does not vary substantially between the different air split conditions. This shift is the result of the variation in air split; as the air split increases, the amount of flow going through the central nozzle increases, resulting in higher shear between the center jet and its surroundings. Additionally, the velocity RMS captures the fluctuations due to the precessing vortex core, which arises at higher air splits, as will be discussed later.

The time-averaged progress variable contour, $\bar{c}$, obtained from the binarized OH-PLIF images is shown in Fig. 5 for varying air split conditions. The black line denotes the $\bar{c} = 0.5$ contour, which is illustrative of the mean flame edge location. In the lower air split cases, the flame is seen to have a distinctive M-shape, stabilizing in both the inner and outer shear layers. As air split increases, the flame detaches from the outer shear layer stabilization point and is largely located in the inner shear layer. This change in flame stabilization is likely the result of the increase in

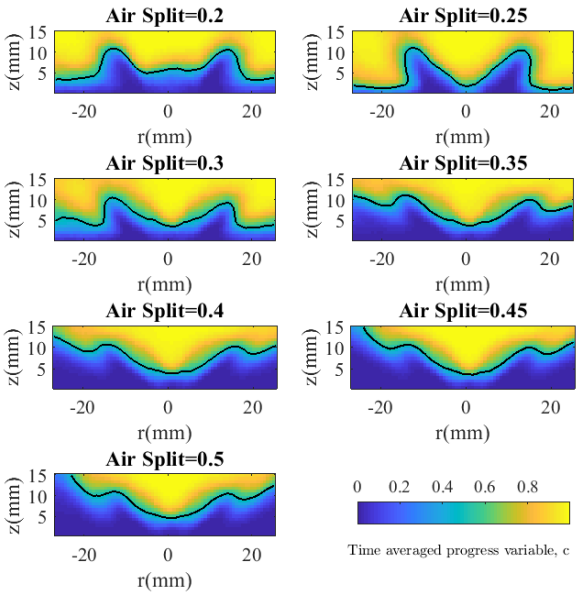

Fig. 5. Time-averaged progress variable contour, $\bar{c}$, for varying air split conditions. Black contour indicates $\bar{c} = 0.5$.

recirculation strength that occurs at higher air splits. As the size and strength of the recirculation zone increases, hot products are drawn into the center of the flow, resulting in favorable conditions for flame stabilization around the recirculation zone rather than in the outer shear layer, as has also been seen in a variable-swirl study by Durox et al. [36].

Thermoacoustic state

The power spectral density of the acoustic pressure for each air split condition is shown in Fig. 6. In the lower air split cases, a strong peak can be seen around 600 Hz. As the air split increases, the 600 Hz peak becomes weaker and a new peak can be seen around 875 Hz. Since the pressure probe is located far downstream of the recirculation zone, both peaks correspond to thermoacoustic modes in the combustor. Additionally, the peak frequencies of the two modes seem to remain largely constant with increasing air split, which is also indicative of a thermoacoustic oscillation mode rather than a hydrodynamic mode, such as the PVC. It has been shown that the frequency of the PVC can scale with varying flow parameters, such as the swirl number or flow velocity [25]. In a complementary study performed using the same data set as this work, we have shown, using spectral analysis and a theoretical formulation, that with increasing air split,

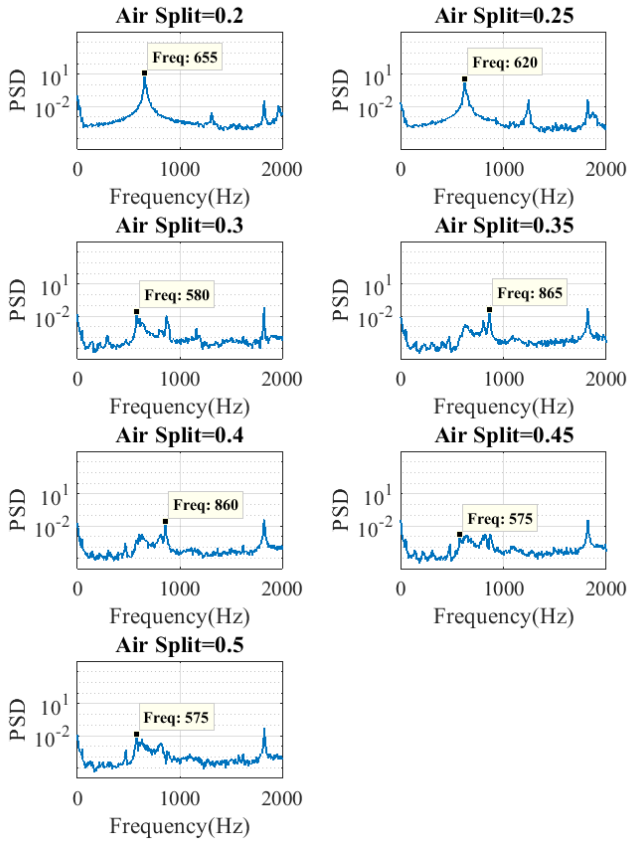

Fig. 6. Power spectral density (kPa^2/Hz) of pressure data at varying air split conditions.

the thermoacoustic mode becomes weaker as a PVC hydrodynamic instability mode increases in strength [30]. The characterization of the nature of oscillation at the peak frequencies is discussed in detail in the coupling mechanism behaviors section.

The level of thermoacoustic oscillation is also characterized by calculating the power spectral density of the flame length variations, as the thermoacoustic oscillation is driven by a coupling between flame heat release rate and pressure, where a major mechanism for flame heat release rate fluctuation is through flame area fluctuation. The flame area is characterized by the total flame length, L_f, defined by equation 1. Figure 7 shows the power spectral density of the fluctuation in flame length at each air split condition. In the low air split cases, the frequency peaks appear at the same frequencies as in the pressure spectra; these are the conditions where the thermoacoustic oscillation is strong. As the air split increases, peaks occur at different frequencies than the thermoacoustic frequency, where the frequency of the peak increases linearly with increasing

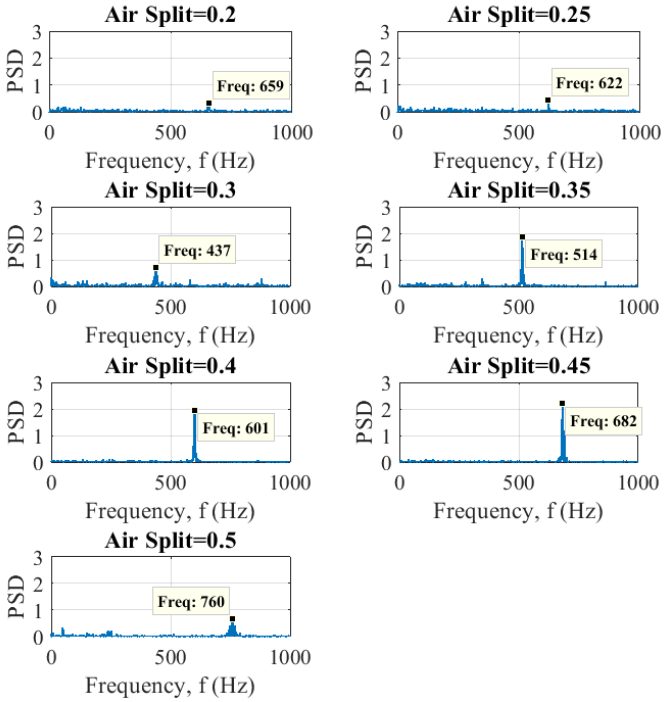

Fig. 7. Power spectral density (in mm^2/Hz) of the total flame length fluctuation L'_f at varying air split conditions.

air split. This frequency behavior is indicative of a hydrodynamic instability mode and is reflected in the analysis of the velocity field [30].

Coupling mechanisms

To understand the coupling mechanisms that drive thermoacoustic instability, we quantitatively analyze the impact of the velocity coupling and equivalence ratio coupling mechanisms on the flame and their interaction with each other.

In order to characterize the velocity coupling mechanism, we perform a Fourier reconstruction (procedure described in Data Analysis section) on the radial velocity component at the peak oscillation frequencies in the velocity spectra; these same frequencies appear in the flame length spectra in Fig. 7. Figure 8 shows snapshot images during one phase of the oscillation of the frequency-filtered, reconstructed radial velocity fields at the two extreme air split conditions. The black contour depicts an instantaneous flame edge (not frequency-filtered) to provide a notional idea of the flame position at these times. It can be seen that in the low air split case, shown on

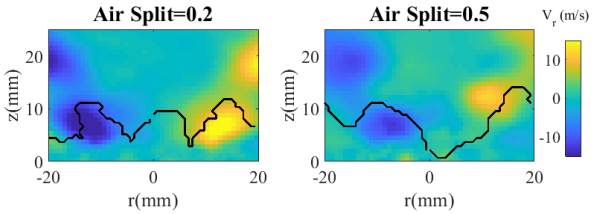

Fig. 8. Snapshots of the Fourier reconstruction of the radial velocity component at the peak oscillation frequency.

the left, the shape of the velocity oscillation mode at the peak frequency is symmetric, and so is the shape of the flame. This result, in conjunction with the combustor pressure measurements, suggest that the dominant oscillation in the low air split case corresponds to the thermoacoustic mode. It is also evident from this image that the flame oscillation is symmetric, as a result of the velocity-coupled response to the thermoacoustic instability.

In the high air split case, shown on the right, the spatial structure of the velocity oscillation mode at the peak frequency is anti-symmetric and resembles the helical vortex shedding that is characteristic of a PVC. It can also be seen that the flame structure is also similarly anti-symmetric, since the flame oscillation is strongly linked to the velocity fluctuations in the region of flame stabilization. The frequency spectra in Fig. 7 and the velocity reconstructions in Fig. 8 show that the flame area fluctuation, and hence the heat release fluctuation, is strongly coupled to the velocity fluctuation. When the dominant velocity fluctuation stems from the thermoacoustic oscillation at low air splits, the flame motion reflects the axisymmetric oscillations. When the dominant velocity fluctuation arises due to the PVC at high air splits, the flame oscillation is also asymmetric.

In order to characterize the fluctuations in fuel flow, we calculate the cross-spectral density of the time series obtained from the left and right branches of the acetone signal taken at the dump plane, which provides a measure of the fuel flow rate at the injection point. Figure 9 shows plots of the cross spectral density, $G_{\psi_R \psi_L}$, on a logarithmic axis, for every air split condition. In all cases, a peak can be seen at the dominant symmetric mode around 600 Hz, the thermoacoustic mode of the combustor, just like the pressure spectra. The phase difference between the left and right signals, calculated from the power spectral density at that peak, is always close to zero degrees, indicating that the predominant fuel flow oscillations are symmetric. In the lower air split

cases, where there is no PVC, we can see a strong the peak corresponding to the thermoacoustic oscillation mode.

At higher air splits, there is still a frequency peak that corresponds to the symmetric mode, based on the phase of $G_{\psi_R\psi_L}$, but the peak is nearly an order of magnitude smaller than in the low air split cases, which indicates significant damping of the thermoacoustic oscillation and hence fuel flow fluctuation. Furthermore, small peaks can be seen at frequencies corresponding to the PVC oscillation. For example, in the air split=0.5 case, the dominant peak is at 577 Hz, which is symmetric (phase difference is 8.48 degrees), but a smaller peak can be seen at the PVC frequency at that condition, at 760 Hz, and the phase difference corresponding to this frequency is 116 degrees, which is closer to out-of-phase, or anti-symmetric, oscillation. This result shows that in the low air split cases, where the thermoacoustic fluctuation is the dominant oscillation in the system, the fuel flow also oscillates symmetrically at the thermoacoustic frequency. As the air split increases and the thermoacoustic oscillation mode weakens, the fuel fluctuation is less coherent but still predominantly symmetric. This trend is likely due to the fact that while a hydrodynamic instability such as the PVC can dampen the thermoacoustic oscillation mode because of its suppression of shear layer oscillations (a process described in detail in Ref. [30]), its influence is limited to the location of the vortex breakdown bubble and its shear layers. As such, the PVC only weakly impacts the fuel flow rate at the fuel-injection point. The thermoacoustic oscillation mode, by contrast, is a system oscillation that creates pressure disturbances throughout the combustor, thereby influencing the fuel injection at the dump plane.

From the analysis of the velocity and equivalence ratio coupling mechanisms, it is seen that while the flame area fluctuations are strongly linked to the velocity field fluctuations, oscillations in the fuel flow are strongly coupled with the thermoacoustic oscillation mode. Oscillations in the fuel flow rate can impact the the rate of heat release by modulating the local equivalence ratio of the flame and hence both the instantaneous heat of combustion and flame speed of the mixture being burnt. To quantify the level of mixture coupling at each condition, we compute the fuel flux to the flame, Φ, defined by Eq. 2, calculated along the instantaneous flame edge at every time instant. Figure 10 shows the power spectral density obtained from the fluctuation in the fuel flux.

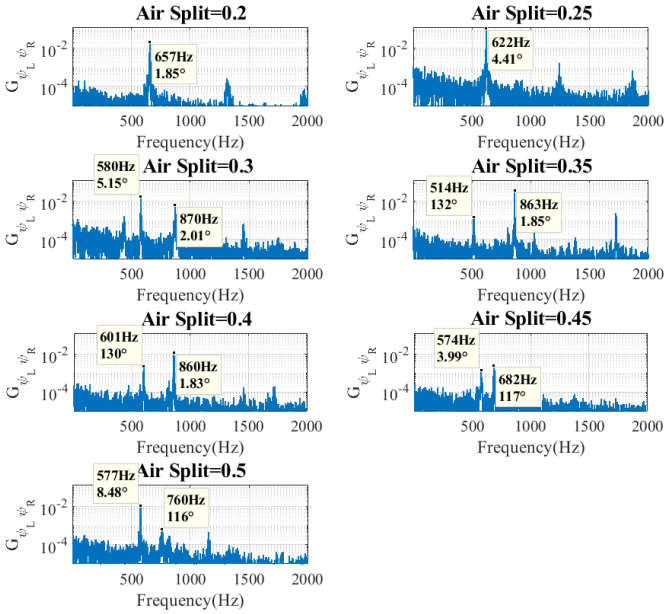

Fig. 9. Magnitude of cross spectral density of the left and right branches of the acetone signal at varying air split conditions. The data labels show the peak frequency and phase difference between the left and right acetone signal time series.

Peaks at the thermoacoustic frequency appear in the lower air split cases and their signal-to-noise ratio is higher than that of the flame length fluctuations in Fig. 7. In the air split=0.5 case, a peak can be seen at the PVC frequency (760 Hz) in addition to the thermoacoustic peak (577 Hz), but the thermoacoustic peak still dominates, though both peaks are low in amplitude compared to the thermoacoustic peaks in the lower air split cases.

This calculation, together with the spectra of the flame fluctuations, is significant, as it illustrates a number of results about flows with both thermoacoustic and hydrodynamic instabilities. First, the combination of fuel flow rate, velocity, fuel flux, and flame area fluctuation results at the low air split conditions indicate that there is a combination of velocity- and mixture-coupling mechanisms driving the thermoacoustic instability. Unfortunately, it is not possible to determine which of the coupling mechanisms plays a larger role in the heat release rate oscillation. Velocity coupling largely acts through flame area fluctuations, whereas mixture coupling drives variations in heat of combustion and flame speed, which then have several secondary effects, all of which drive the heat release rate oscillations. Decomposing these different contributions is not possible with experimental data as a direct measurement of heat release rate is not available. What can be

said, though, is that both these coupling mechanisms are present as this is a partially-premixed configuration.

Additionally, there is likely a coupling between the velocity- and mixture-coupling mechanisms that drives the high levels of fuel flux fluctuations when the thermoacoustic instability is strong. This result is evidenced by the coherent oscillations of the velocity field, the fuel injection rate, and the fuel flux at the flame edge all together. However, the PVC-driven velocity oscillations do not result in strong coupling with the mixture-coupling mechanism. This result is evidenced by both the lack of fuel flow fluctuation at the PVC frequency at the fuel injection location as well as the weak fuel flux fluctuations at the flame edge when a PVC is present. Although the flame length fluctuations at the PVC frequency are large at high air splits, these oscillations do not drive a thermoacoustic mode or enhanced fuel flux to the flame. Previous work on helical instabilities has shown that, in the compact-flame regime, they do not result in net heat release rate oscillations, which makes them unlikely to drive thermoacoustic instabilities [37, 38]. As such, when the velocity-coupling mechanism is suppressed by the PVC, the mixture-coupling mechanism is not dominant enough to drive the thermoacoustic instability by itself; the thermoacoustics are suppressed when the velocity coupling disappears.

CONCLUSIONS

The focus of this work is to understand and characterize the interaction between the velocity-coupling mechanism, driven by a large-scale vortical oscillations, the mixture-coupling mechanism, driven by fluctuation in the fuel flow rate, and their impact on the structure of the flame. The role of the PVC in stabilization of turbulent flames has been the subject of several experimental studies. In many configurations, it has been shown that the PVC enhances the static stability of flame by promoting the mixing of fuel and air [9, 39–41]. In this work, we show that this is not universally true. In particular, the influence of the PVC is spatially limited to the location of the recirculation zone and if the PVC is sufficiently far downstream of the fuel injection location, it will have no direct impact on the fuel fluctuation or the flux of reactants into the flame. The thermoacoustic oscillation mode, however, is a system oscillation that creates coherent pressure fluctuations

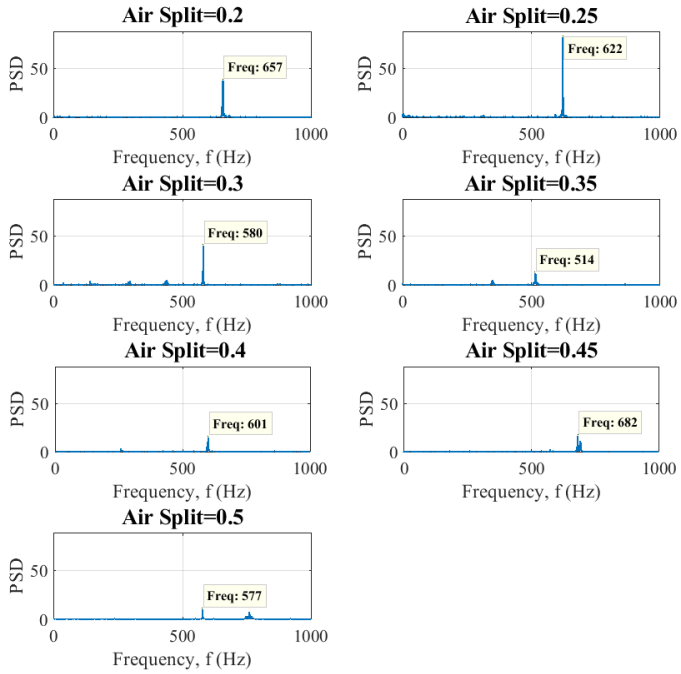

Fig. 10. Power spectral density of the fluctuation in fuel flux Φ' at varying air split conditions.

throughout the combustor and directly impacts the fluctuation of fuel flow at the injection location. However, the PVC indirectly influences the fuel fluctuation by suppressing thermoacoustic oscillation.

Our analysis shows that the structure of the flame is strongly coupled to the oscillation of the PVC, as the flame is stabilized in the shear layers around the recirculation zone. This finding is consistent with the results reported in the literature. Ultimately, we show, using a characterization of the flame, fuel, and flow behavior, that in a case where the PVC and the fuel injection location are sufficiently separated, the velocity coupling and the equivalence ratio coupling mechanisms do not interact with each other, as seen in the high air split cases here. Since this study was performed on a data set from a realistic, swirl-stabilized, model combustor, the results presented here can inform design of gas turbine engine combustors and provide insight into the mechanics of thermoacoustic instability suppression and control.

ACKNOWLEDGEMENTS

This work was supported by National Science Foundation grant CBET-1749679 and Air Force Office of Scientific Research grant FA9550-16-1-0044. Any opinions, findings, and conclusions or recommendations expressed in this material are those of the authors and do not necessarily reflect the views of the National Science Foundation or the Air Force Office of Scientific Research. The assistance of Dr. Jisu Yoon (ADD, Republic of Korea), Dr. Carrie Noren (AFRL, USA), and Dr. Klaus-Peter Geigle (DLR, Germany) with the setup and operation of the experimental apparatus described in this paper are gratefully acknowledged.

REFERENCES

[1] Lieuwen, T. C., and Yang, V., 2005. *Combustion instabilities in gas turbine engines: operational experience, fundamental mechanisms, and modeling*. American Institute of Aeronautics and Astronautics.

[2] Ducruix, S., Schuller, T., Durox, D., and Candel, S., 2003. "Combustion dynamics and instabilities: elementary coupling and driving mechanisms". *Journal of Propulsion and Power,* **19**(5), pp. 722–734.

[3] Lieuwen, T., and Zinn, B. T., 1998. "The role of equivalence ratio oscillations in driving combustion instabilities in low nox gas turbines". In Symposium (International) on Combustion, Vol. 27, pp. 1809–1816.

[4] Kim, K. T., Lee, J. G., Quay, B. D., and Santavicca, D., 2010. "Response of partially premixed flames to acoustic velocity and equivalence ratio perturbations". *Combustion and Flame,* **157**(9), pp. 1731–1744.

[5] Shreekrishna, Hemchandra, S., and Lieuwen, T., 2010. "Premixed flame response to equivalence ratio perturbations". *Combustion Theory and Modelling,* **14**(5), pp. 681–714.

[6] Auer, M., Hirsch, C., and Sattelmayer, T., 2006. "Influence of air and fuel mass flow fluctuations in a premix swirl burner on flame dynamics". In ASME Turbo Expo 2006: Turbine Technical Conference and Exposition, American Society of Mechanical Engineers Digital Collection.

[7] Bluemner, R., Paschereit, C. O., and Oberleithner, K., 2019. "Generation and transport of equivalence ratio fluctuations in an acoustically forced swirl burner". *Combustion and Flame,* **209**, pp. 99–116.

[8] Lee, J. G., Kim, K., and Santavicca, D., 2000. "Measurement of equivalence ratio fluctuation and its effect on heat release during unstable combustion". *Proceedings of the Combustion Institute,* **28**(1), pp. 415–421.

[9] Stöhr, M., Arndt, C. M., and Meier, W., 2015. "Transient effects of fuel–air mixing in a partially-premixed turbulent swirl flame". *Proceedings of the Combustion Institute,* **35**(3), pp. 3327–3335.

[10] Paschereit, C. O., Gutmark, E., and Weisenstein, W., 1999. "Coherent structures in swirling flows and their role in acoustic combustion control". *Physics of Fluids,* **11**(9), pp. 2667–2678.

[11] Gonzalez, E., Lee, J., and Santavicca, D., 2005. "A study of combustion instabilities driven by flame-vortex interactions". In 41st AIAA/ASME/SAE/ASEE Joint Propulsion Conference & Exhibit.

[12] Poinsot, T. J., Trouve, A. C., Veynante, D. P., Candel, S. M., and Esposito, E. J., 1987. "Vortex-driven acoustically coupled combustion instabilities". *Journal of Fluid Mechanics,* **177**, pp. 265–292.

[13] Shanbhogue, S., Shin, D.-H., Hemchandra, S., Plaks, D., and Lieuwen, T., 2009. "Flame-sheet dynamics of bluff-body stabilized flames during longitudinal acoustic forcing". *Proceedings of the Combustion Institute,* **32**(2), pp. 1787–1794.

[14] Kang, D., Culick, F., and Ratner, A., 2007. "Combustion dynamics of a low-swirl combustor". *Combustion and Flame,* **151**(3), pp. 412–425.

[15] Renard, P.-H., Rolon, J. C., Thévenin, D., and Candel, S., 1999. "Investigations of heat release, extinction, and time evolution of the flame surface, for a nonpremixed flame interacting with a vortex". *Combustion and Flame,* **117**(1-2), pp. 189–205.

[16] Lee, T.-W., Lee, J., Nye, D., and Santavicca, D., 1993. "Local response and surface properties of premixed flames during interactions with kármán vortex streets". *Combustion and Flame,* **94**(1-2), pp. 146–160.

[17] Ghoniem, A. F., and Givi, P., 1988. "Lagrangian simulation of a reacting mixing layer at low heat release". *AIAA Journal,* **26**(6), pp. 690–697.

[18] Harvey, J., 1962. "Some observations of the vortex breakdown phenomenon". *Journal of Fluid Mechanics,* **14**(4), pp. 585–592.

[19] Lucca-Negro, O., and O'Doherty, T., 2001. "Vortex breakdown: a review". *Progress in Energy and Combustion Science,* **27**(4), pp. 431–481.

[20] Brown, G., and Lopez, J., 1990. "Axisymmetric vortex breakdown part 2. physical mechanisms". *Journal of Fluid Mechanics,* **221**, pp. 553–576.

[21] Syred, N., 2006. "A review of oscillation mechanisms and the role of the precessing vortex core (pvc) in swirl combustion systems". *Progress in Energy and Combustion Science,* **32**(2), pp. 93–161.

[22] Syred, N., and Beer, J., 1974. "Combustion in swirling flows: a review". *Combustion and Flame,* **23**(2), pp. 143–201.

[23] Ruith, M. R., Chen, P., Meiburg, E., and Maxworthy, T., 2003. "Three-dimensional vortex breakdown in swirling jets and wakes: direct numerical simulation". *Journal of Fluid Mechanics,* **486**, p. 331–378.

[24] Oberleithner, K., Stöhr, M., Im, S. H., Arndt, C. M., and Steinberg, A. M., 2015. "Formation and flame-induced suppression of the precessing vortex core in a swirl combustor: Experiments and linear stability analysis". *Combustion and Flame,* **162**(8), pp. 3100–3114.

[25] Manoharan, K., Frederick, M., Clees, S., O'Connor, J., and Hemchandra, S., 2020. "A weakly nonlinear analysis of the precessing vortex core oscillation in a variable swirl turbulent round jet". *Journal of Fluid Mechanics,* **884**, p. A29.

[26] Stöhr, M., Boxx, I., Carter, C. D., and Meier, W., 2012. "Experimental study of vortex-flame interaction in a gas turbine model combustor". *Combustion and Flame,* **159**(8), pp. 2636–2649.

[27] Frederick, M., Manoharan, K., Dudash, J., Brubaker, B., Hemchandra, S., and O'Connor, J., 2018. "Impact of precessing vortex core dynamics on shear layer response in a swirling jet". *Journal of Engineering for Gas Turbines and Power,* **140**(6), p. 061503.

[28] Steinberg, A. M., Boxx, I., Stöhr, M., Carter, C. D., and Meier, W., 2010. "Flow–flame interactions causing acoustically coupled heat release fluctuations in a thermo-acoustically unstable gas turbine model combustor". *Combustion and Flame,* **157**(12), pp. 2250–2266.

[29] Moeck, J. P., Bourgouin, J.-F., Durox, D., Schuller, T., and Candel, S., 2012. "Nonlinear interaction between a precessing vortex core and acoustic oscillations in a turbulent swirling flame". *Combustion and Flame,* **159**(8), pp. 2650–2668.

[30] Karmarkar, A., Gupta, S., Boxx, I., Hemchandra, S., and O'Connor, J., 2020. "Impact of precessing vortex core dynamics on the thermoacoustic instabilities in a swirl stabilized combustor". *arXiv:2011.14662*.

[31] Geigle, K. P., Köhler, M., O'Loughlin, W., and Meier, W., 2015. "Investigation of soot formation in pressurized swirl flames by laser measurements of temperature, flame structures and soot concentrations". *Proceedings of the Combustion Institute,* **35**(3), pp. 3373–3380.

[32] Stöhr, M., Yin, Z., and Meier, W., 2017. "Interaction between velocity fluctuations and equivalence ratio fluctuations during thermoacoustic oscillations in a partially premixed swirl combustor". *Proceedings of the Combustion Institute,* **36**(3), pp. 3907–3915.

[33] Fugger, C. A., Roy, S., Caswell, A. W., Rankin, B. A., and Gord, J. R., 2019. "Structure and dynamics of ch2o, oh, and the velocity field of a confined bluff-body premixed flame, using simultaneous plif and piv at 10 khz.". *Proceedings of the Combustion Institute,* **37**(2), pp. 1461–1469.

[34] Steinberg, A. M., Boxx, I., Arndt, C., Frank, J. H., and Meier, W., 2011. "Experimental study of flame-hole reignition mechanisms in a turbulent non-premixed jet flame using sustained multi-khz piv and crossed-plane oh plif". *Proceedings of the Combustion Institute,* **33**(1), pp. 1663–1672.

[35] Trunk, P. J., Boxx, I., Heeger, C., Meier, W., Böhm, B., and Dreizler, A., 2013. "Premixed flame propagation in turbulent flow by means of stereoscopic piv and dual-plane oh-plif at sustained khz repetition rates". *Proceedings of the Combustion Institute,* **34**(2), pp. 3565–3572.

[36] Durox, D., Moeck, J. P., Bourgouin, J.-F., Morenton, P., Viallon, M., Schuller, T., and Candel, S., 2013. "Flame dynamics of a variable swirl number system and instability control".

Combustion and Flame, **160**(9), pp. 1729–1742.

[37] Acharya, V., Shin, D.-H., Lieuwen, T., et al., 2012. "Swirl effects on harmonically excited, premixed flame kinematics". *Combustion and Flame,* **159**(3), pp. 1139–1150.

[38] O'Connor, J., and Lieuwen, T., 2012. "Further characterization of the disturbance field in a transversely excited swirl-stabilized flame". *Journal of Engineering for Gas Turbines and Power,* **134**(1).

[39] Freitag, M., Klein, M., Gregor, M., Geyer, D., Schneider, C., Dreizler, A., and Janicka, J., 2006. "Mixing analysis of a swirling recirculating flow using dns and experimental data". *International Journal of Heat and Fluid Flow,* **27**(4), pp. 636 – 643.

[40] Galley, D., Ducruix, S., Lacas, F., and Veynante, D., 2011. "Mixing and stabilization study of a partially premixed swirling flame using laser induced fluorescence". *Combustion and Flame,* **158**(1), pp. 155–171.

[41] Lückoff, F., and Oberleithner, K., 2019. "Excitation of the precessing vortex core by active flow control to suppress thermoacoustic instabilities in swirl flames". *International Journal of Spray and Combustion Dynamics,* **11**, pp. 1–23.